Detailed analysis of the crystallization of the Co-P amorphous system: Kinetics, influence of magnetic order, and formation of textures

F. Cebollada
Departamento de Física Aplicada, EUIT de Telecomunicación, Universidad Politécnica de Madrid, c/Camino de la Arboleda s/n, 28031 Madrid, Spain

J. M. González and C. de Julián
Instituto de Ciencia de Materiales, CSIC, 28049 Cantoblanco, Madrid, Spain

S. Suriñach
Departament de Física, Universitat Autònoma de Barcelona, 08193 Bellaterra, Spain
(Received 20 November 1996)

The crystallization kinetics of the amorphous Co-P system and the influence of the magnetic order of the samples on the microstructural and magnetic features of the crystallization product have been studied. By assuming an additive kinetics, the calculated temperature-time-transformation (T-T-T) and temperature–heating-rate–transformation (T-HR-T) curves are in good agreement with the experimental data. Scanning electron microscopy, x-ray diffraction, and magnetic measurements show that a clear texture is induced and that the easy axis of the amorphous samples is preserved during the crystallization process for samples with the Curie temperature well above the crystallization temperature. This clearly shows that magnetic order plays an important role in the crystallization in this system. [S0163-1829(97)05834-7]

I. INTRODUCTION

Detailed knowledge of the crystallization kinetics of amorphous metallic alloys is important since it yields the conditions under which these materials can be used preventing their crystallization, i.e., preventing dramatic changes in many physical properties that might be of interest (e.g., resistivity, elastic or magnetic properties).[1] In addition to this, the crystallization of amorphous precursors gives rise to microstructures that may be difficult to obtain using conventional methods in specific systems. By using this approach microstructural features useful for given technological applications (e.g., well-defined crystalline textures, homogeneous grain size distribution, etc.) may be produced.[2] From a more fundamental point of view, the crystallization of amorphous systems provides a useful tool to obtain information about the mechanism of atom diffusion and crystal nucleation and growth in an isotropic medium.

Co-P alloys with a wide variety of physical features can be easily prepared by electrodeposition, which allows a precise control of their structural and magnetic properties. In fact, by varying the temperature of the electrolytic bath and the cathode current density, either polycrystalline or amorphous alloys in a wide composition range, as well as compositionally modulated structures, can be prepared.[3,4] In particular, Co-P amorphous alloys, prepared using this technique, have a highly homogeneous composition, magnetic properties, and distribution of residual stresses, compared to amorphous alloys obtained by rapid solidification.

Electrodeposited amorphous Co-P alloys are characterized by uniaxial anisotropy, with the easy axis being perpendicular to the plane of the samples. Thus the in-plane hysteresis curves show an almost constant differential susceptibility region until saturation is reached, yielding a very-well-defined anisotropy field of the order of 100 Oe.[5,6] The origin of this anisotropy lies in the internal shape factor due to growth in the deposition process of Co-rich elongated ellipsoidal regions perpendicular to the plane of the samples.[7,8] It is even possible to switch this perpendicular-to-the-plane anisotropy to in-plane anisotropy by using a rotating substrate during the sample preparation procedure,[9] which provides this system with a large versatility for tailoring its magnetic anisotropy.

Although the magnetic anisotropy in these alloys is almost independent of their composition (from 10 at. % P to about 30 at. % P), a significant change in their Curie temperatures (from 750 K for 19 at. % P to 530 K for 24 at. % P) was observed.[10] Although the presence of the previously mentioned Co-rich ellipsoidal regions, which are of the order of 1000 Å long and 100 Å wide,[7,8] rules out microscopic compositional homogeneity, the electrodeposited Co-P alloys are highly homogeneous macroscopically. In fact, energy-dispersive x-ray (EDX) analysis has shown that the local composition (within a few micrometers resolution) remains constant throughout most of the sample, with a slight increase in the average Co content in the regions close to the edges of the samples.[11]

We must point out that it is this high homogeneity and the wide Curie temperature and composition ranges attainable for this amorphous system that make it suitable for a detailed analysis of its crystallization kinetics and also of the influence of magnetic order on its crystallization. This contrasts with melt-spun amorphous ribbons, in which regions with both tensile and compressive residual stresses are inhomogeneously distributed, usually leading (via magnetoelastic coupling) to the appearance of different regions with either in-plane and perpendicular-to-the plane magnetic anisotropy.[12]

Although the crystallization process of the Co-P amor-

phous system has been studied earlier,[13–18] both directly (calorimetric measurements) and indirectly (through the evolution of structurally sensitive properties such as resistivity or coercive force), most of them were restricted to partial aspects. In fact, some of them just determine the crystallization temperatures of a few alloys and study the microstructural features of the resulting crystallization products.[13] Others are based on the assumption that the relative variation of a given physical property is proportional to the crystallized fraction α, which is not obvious, and go as far as determining the Avrami index n by means of the conventional $\ln[-\ln(1-\alpha)]$ vs $\ln t$ plots.[14,15]

In this work we present results on the crystallization kinetics of the Co-P amorphous system (P between 10 and 24 at. %), covering a wide spectrum of saturation magnetization, Curie and crystallization temperatures. The magnetic measurements and microstructural observations revealed the formation of a strong texture, preserving the columnar structure of the amorphous precursors for the samples with the Curie temperature well above the crystallization temperature. On the contrary, an isotropic distribution of crystallites (similar to that of crystalline electrodeposited Co-P alloys) was observed upon crystallization of the samples with Curie temperature below that of crystallization. All data strongly support the conjecture that the presence of magnetic order acts as a polarizing agent for the diffusion of Co atoms during the crystallization process.

II. SAMPLES AND EXPERIMENTAL TECHNIQUES

Samples of composition $Co_{100-x}P_x$ ($10<x<25$) were prepared by electrodeposition by using a standard electrolytic bath,[3] at 353 K, and current densities ranging from 500 to 6×10^3 A m^{-2}. Rectangular polished Cu foils (50×10 mm^2) were used as substrates and removed by electrolytic etching after deposition. The thickness of the samples was approximately 50 μm except for those with the highest P contents (obtained using the lowest current densities), which were $\sim$20 μm thick. The chemical composition of the samples was analyzed by means of two complementary techniques. The local composition was studied by EDX analysis, with 1 μm resolution, which showed that there is an increase of a few percent in the Co content when close ($\sim$1–2 mm) to the edges of the samples. The global composition of the central region of the samples was also analyzed by plasma emission spectroscopy, showing good agreement with the EDX results. In order to avoid the effect of this compositional inhomogeneity,[11] only pieces cut out from the central region were used in all studies.

The heat treatments and calorimetric measurements were performed by means of isothermal and continuous heating scans (10–80 K min^{-1}) in a Perkin-Elmer scanning microcalorimeter, model DSC-7. The microstructural studies were carried out by scanning electron microscopy (SEM) using a JEOL 840 electron microscope, on freshly fractured surfaces, and by x-ray diffraction (XRD), using a Siemens D 500 diffractometer and Cu $K\alpha$ radiation. The magnetic measurements were done in a vibrating sample magnetometer (PAR 155) on disk-shaped specimens of 6 mm diameter. The maximum applied field was 0.5 T.

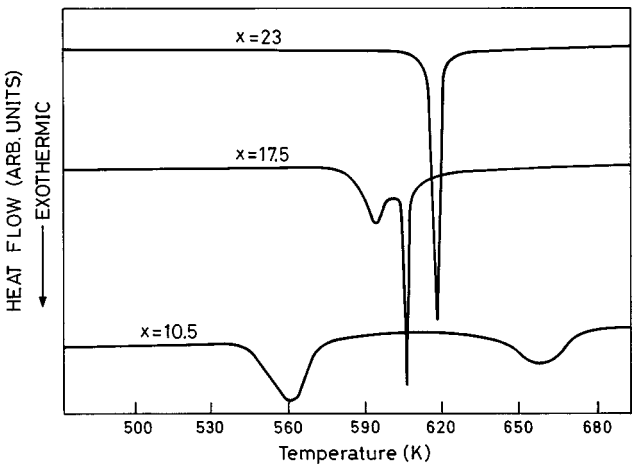

FIG. 1. DSC curves recorded at a heating rate of 10 K min^{-1} for three samples of different composition.

III. CRYSTALLIZATION KINETICS: EXPERIMENTAL RESULTS AND ANALYSIS

The crystallization temperature of all samples was determined from continuous heating differential scanning calorimetry (DSC) curves carried out at several heating rates. These curves exhibit two clearly different behaviors depending on the composition: samples with $x>21$ manifest a single crystallization peak, while those with $x<21$ crystallize in two consecutive steps that are not always fully resolvable (Fig. 1). Subsequent DSC runs, up to 990 K, of previously crystallized samples showed no traces of any other peak, which indicates that the crystalline phases produced are stable up to that temperature.

Figure 2 presents the compositional dependence of the temperature of the maximum of the crystallization peaks (data correspond to a heating rate of 10 K min^{-1}), as well as that of the Curie temperature (data taken from Ref. 10). Each one of these two types of behavior can be correlated to a particular type of microstructure and of magnetic hysteresis behavior in the resulting crystallization product (see below).

In order to analyze the crystallization in this system, we

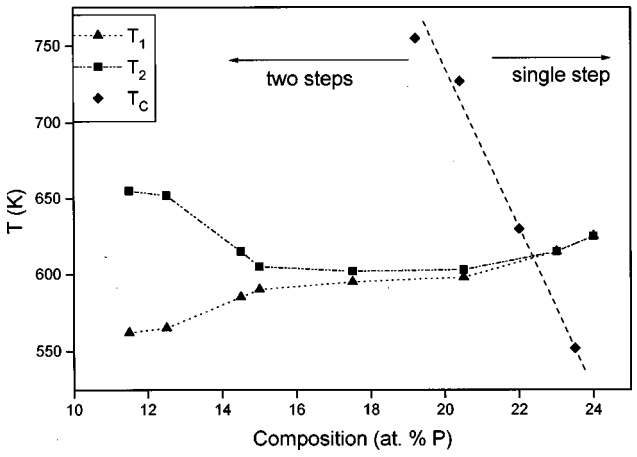

FIG. 2. Compositional dependence of the temperature corresponding to the maxima of the crystallization peaks (T_1 and T_2), from DSC scans at 10 K min^{-1}, and of the Curie temperature (T_c).

have assumed (for each crystallization step) that an additive kinetic holds, that is, that the transformation rate is a function of temperature and of a previously crystallized fraction, independently of the history of the sample. The crystallization rate $d\alpha/dt$ is then given by

$$d\alpha/dt = k(T)f(\alpha), \tag{1}$$

where α is the crystallization fraction.

The $f(\alpha)$ reflects the particular crystallization mechanism of the samples and is usually described by the Johnson-Mehl-Avrami (JMA) model[19,20]

$$f(\alpha) = n(1-\alpha)[-\ln(1-\alpha)]^{(n-1)/n}. \tag{2}$$

The Avrami index n typically ranges from 0.5 to 4 and depends on the conditions of nucleation and growth (e.g., homogeneous or preferential nucleation, isotropic or anisotropic growth mode, etc.) However, any study of the crystallization kinetics which is limited to the determination of the value of the Avrami index does not provide sufficient information to determine the crystallization mechanism.[21] In fact, different nucleation and growth mechanisms may simultaneously happen in the crystallization process, thus making impossible the description of $f(\alpha)$ by means of a single JMA-type function. In this case, experimentally obtained $f(\alpha)$ functions may be used.

$k(T)$ is usually described by an Arrhenius-type relation

$$k(T) = A\ \exp(-E/K_B T), \tag{3}$$

where A is the frequency factor, E the activation energy, K_B the Boltzmann constant, and T the absolute temperature.

The integration of Eq. (1),

$$\int_0^t k(T)dt = \int_0^\alpha d\alpha/f(\alpha) = g(\alpha), \tag{4}$$

can be performed numerically using a standard procedure.[22] The temperature-time-transformation (T-T-T) curves and the crystallized fraction $\alpha = \alpha(T,t)$ can be obtained considering isothermal conditions. The temperature–heating-rate–transformation (T-HR-T) curves and $\alpha = \alpha(T,r)$ can also be calculated for heating at a constant rate $r = T/t$. In both types of curves, the crystallized fraction α is used as a parameter and some values corresponding to the initial (e.g., $\alpha = 0.01$), intermediate (e.g., $\alpha = 0.50$), and final (e.g., $\alpha = 0.99$) part of the crystallization process, respectively, are usually sufficient to describe adequately the crystallization kinetics of a system.

In order to perform the integration (4), the $f(\alpha)$ function must be previously calculated, which is accomplished through the expression

$$\ln[Af(\alpha)] = \ln[d\alpha/dt] + E/K_B T, \tag{5}$$

deduced from Eqs. (1) and (3). This, in turn, requires knowledge of the transformation rate $d\alpha/dt$ and of the activation energy of the sample, E, which can be obtained from the Kissinger plots.[23] The $d\alpha/dt$ values can be provided by a single DSC scan and are directly given by the height of the curve at each time divided by its total area.

Table I shows the values of the activation energies corresponding to the first and second crystallization steps for the samples of different compositions. These values were calculated from Kissinger plots from four DSC scans at 10, 20, 40, and 80 K min^{-1}. The samples with P content below 21 at. % present values close to 1.8 and 1.9 eV for the first and second steps, respectively, while the single crystallization step of the samples with $x > 21$ has an activation energy of 1.95 eV. The values of the frequency factor A, estimated using the procedure outlined in the Appendix, are also shown in Table I. As can be seen, those corresponding to the first and second steps of the samples with $x < 21$ are of the order of 10^{14} and 10^{13} s^{-1}, respectively. For the samples with $x > 21$, the frequency factors are of the order of 10^{14} s^{-1}.

TABLE I. Activation energy (E) and estimation of the frequency factor (A) for the first and second crystallization steps of different Co-P samples.

	E (eV)			A (s^{-1})		
Composition (x)	First step	Single step	Second step	First step	Single step	Second step
23.0		1.95			3.5×10^{13}	
17.5	1.89		1.85	2.9×10^{14}		2.9×10^{13}
12.5	1.78		1.84	9.8×10^{13}		1.9×10^{13}
11.5	1.76		2.01	1.5×10^{14}		2.3×10^{13}
10.5	1.76		2.02	1.9×10^{14}		2.5×10^{13}

As previously mentioned, $f(\alpha)$ can be calculated using the $d\alpha/dT$ values obtained from a single DSC curve and the activation energy E. In our study we calculated different $f(\alpha)$ functions corresponding to samples of compositions given by $x = 10.5$, 11.5, 12.5, and 17.5 using a DSC scan at 10 K/min^{-1} for each composition and crystallization step. Figures 3 and 4 show the $\ln[Af(\alpha)]$ versus $-\ln[(1-\alpha)]$ plots for the first and second steps, respectively. We did not include the data corresponding to the sample with $x = 17.5$ here

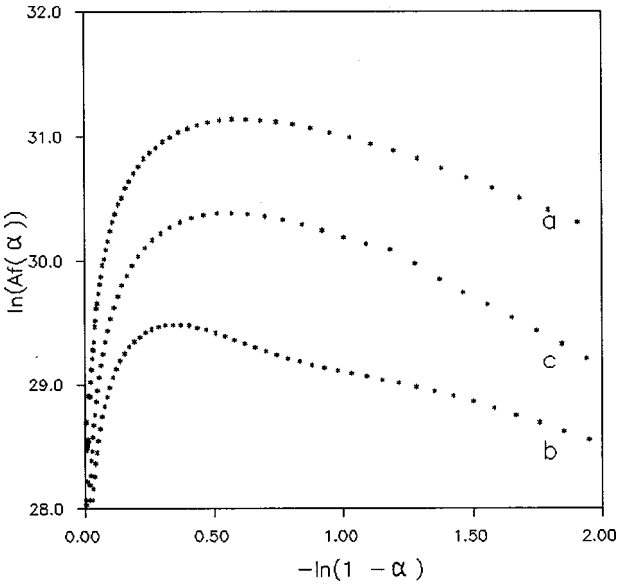

FIG. 3. First crystallization step: $\ln[Af(\alpha)]$ vs $-\ln(1-\alpha)$ plot for the samples with $x = 10.5$ (a), 11.5 (b), and 12.5 (c), respectively. This plot is not consistent with fitting $f(\alpha)$ to Eq. (2) using a single n value.

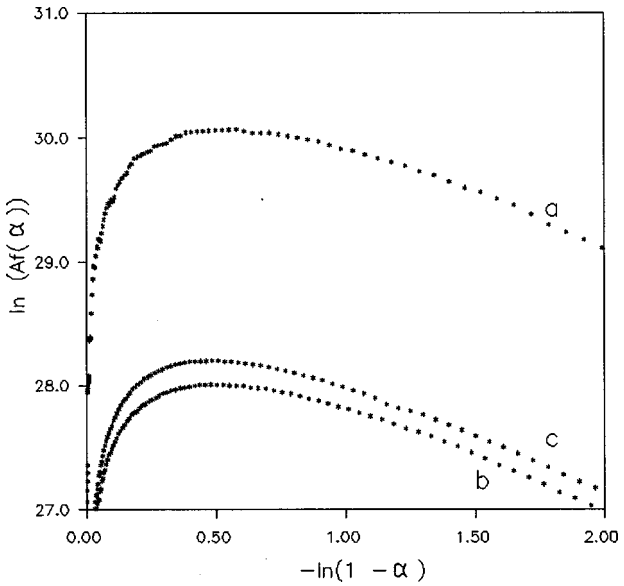

FIG. 4. Second crystallization step: $\ln[Af(\alpha)]$ vs $-\ln(1-\alpha)$ plot for the samples with $x=10.5$ (a), 11.5 (b), and 12.5 (c), respectively. Similarly to Fig. 3, this plot is not consistent with fitting $f(\alpha)$ to Eq. (2) using a single n value.

since we could not treat both crystallization steps separately. From these plots we could infer that it is not possible to fit the $f(\alpha)$ function to expression (2) using a single Avrami index n for the full α range (0–1).

Once $f(\alpha)$ was obtained, the integration of Eq. (4) can be performed. Under isothermal conditions this is straightforward,

$$g(\alpha)=A\ \exp(-E/K_BT)t, \tag{6}$$

and yields the T-T-T curves. Figures 5 and 6 show these curves for two samples with $x=11.5$ and 17.5.

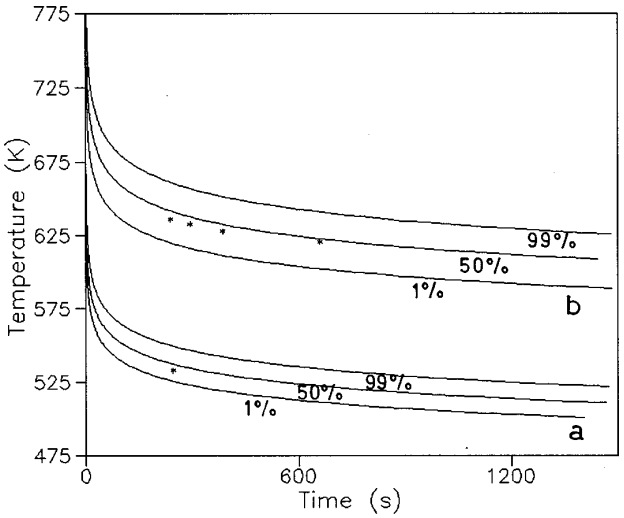

FIG. 5. Calculated temperature-time-transformation (T-T-T) diagrams corresponding to different crystallized fractions of the first (a) and second (b) steps of a sample with $x=11.5$. The experimental points were obtained from isothermal DSC scans at different temperatures, and all of them correspond to a crystallized fraction of 50%.

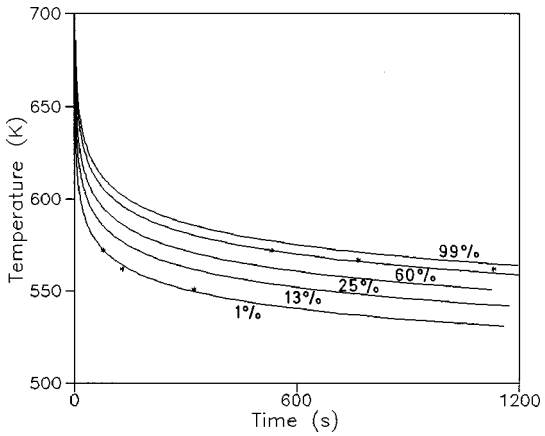

FIG. 6. Calculated temperature-time-transformation (T-T-T) diagrams for different crystallized fractions of a sample with $x=17.5$ and experimental points obtained from isothermal DSC scans at different temperatures. These points correspond to crystallized fraction values of 13% and of 60%. The points corresponding to $\alpha=13\%$ lie near the 1% T-T-T curve, while those corresponding to $\alpha=60\%$ lie near the 60% T-T-T curve.

Several DSC isothermal scans at different temperatures were performed in order to check the validity of these calculated curves. As an example, Fig. 7 presents three scans corresponding to the second step carried out on samples with $x=11.5$ at different temperatures. By taking the time required at each temperature to achieve a crystallized fraction of 50%, the experimental points appearing in the upper curves (corresponding to the second step) of Fig. 5 were obtained. The point in the lower curves (first step) was obtained in a similar way and also corresponds to a crystallized fraction of 50%. For all compositions allowing separation of both crystallization steps, good agreement was observed between the experimental points and the calculated T-T-T curves.

On the other hand, when full separation of the crystallization peaks was not possible, the agreement was good just for large values of the crystallized fraction. The experimental (t,T) points appearing in Fig. 6 were obtained, by means of the procedure explained in the previous paragraph, from iso-

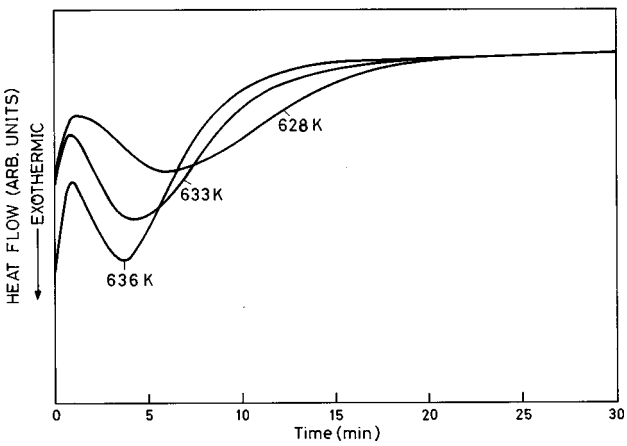

FIG. 7. Isothermal DSC scans recorded at three different temperatures (all corresponding to the second crystallization step) for samples of composition given by $x=11.5$.

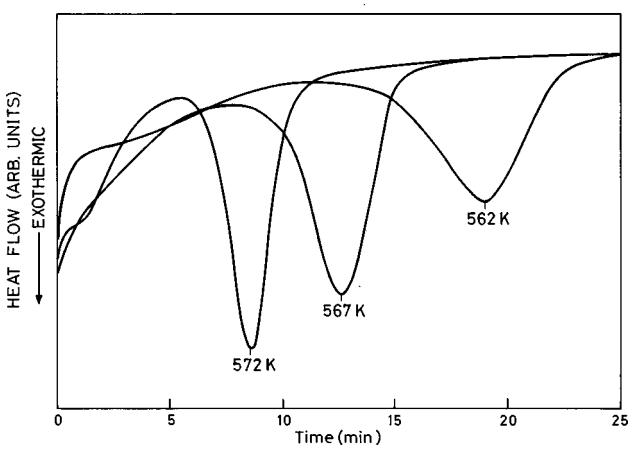

FIG. 8. Isothermal DSC scans recorded at three different temperatures for samples of composition given by $x=17.5$.

thermal scans carried out at different temperatures on samples with $x=17.5$ (Fig. 8). Although the three lower points correspond to a crystallized fraction of 13%, they are placed on the calculated curve corresponding to $\alpha=1\%$ (that is, they should lie on the curve immediately above). However, the three upper points correspond to a crystallized fraction of 60% and lie on the calculated 60% curve; that is, there is good agreement between the experimental points and the calculated curve.

Under continuous heating at a constant rate r, Eq. (4) becomes

$$(A/r)\int_0^T \exp[-E/K_BT]dT=g(\alpha) \tag{7}$$

and the integration of this equation was carried out by approximating the integral between 0 and T.[24] The following expression was then deduced:

$$g(\alpha)=(AK_BT^2/rE)\exp(-E/K_BT), \tag{8}$$

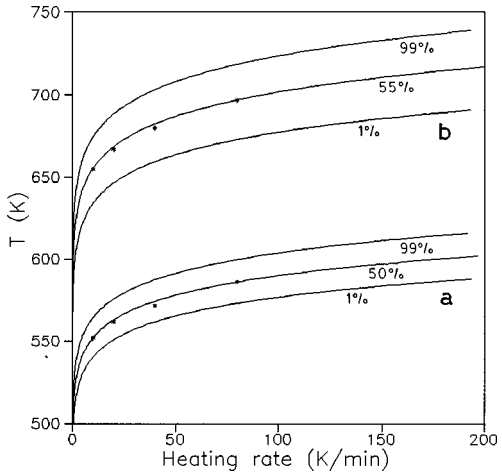

FIG. 9. Calculated temperature–heating-rate–transformation (T-HR-T) diagrams corresponding to different crystallized fractions of the first (a) and second (b) step of a sample with $x=11.5$ and experimental points obtained from continuous heating DSC scans. These points correspond to a crystallized fraction value of 50%, for the first step, and of 55%, for the second step.

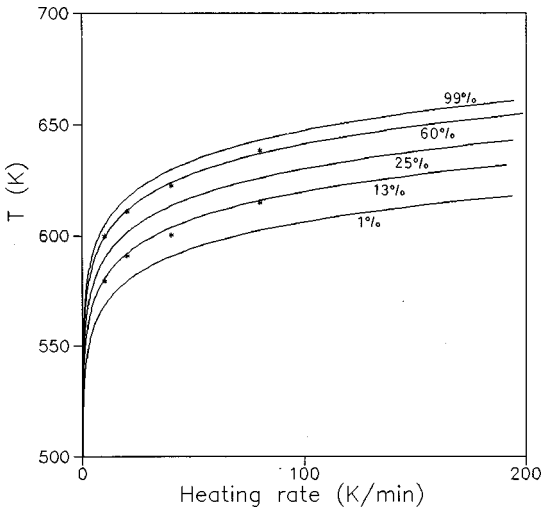

FIG. 10. Calculated temperature–heating-rate–transformation (T-HR-T) diagrams corresponding to different crystallized fractions of a sample with $x=17.5$ and experimental points obtained from continuous heating DSC scans. At each scanning rate the experimental points correspond to crystallized fraction values of 13% and 60%, respectively.

from which the T-HR-T curves can be obtained. The calculated curves for a composition given by $x=11.5$ are presented in Fig. 9, where the lower (upper) curves correspond to the first (second) crystallization step.

In order to check the validity of these curves, experimental points were also obtained. The temperatures required to reach a crystallized fraction of 50% (for the first step) and of 55% (for the second step) in samples with $x=11.5$ were obtained at different heating rates (10, 20, 40, and 80 K min^{-1}). Good agreement between the experimental points and the calculated curves was observed (see Fig. 9).

Figure 10 exhibits several calculated T-HR-T curves corresponding to a composition given by $x=17.5$. The experimental points were produced by means of the procedure outlined above and correspond to the temperatures required to reach crystallized fractions of 13% and 60%, respectively, for each heating rate. Good agreement between the experimental points and the calculated curves was also found.

IV. MICROSTRUCTURAL ANALYSIS

Samples with $x<21$ exhibit two consecutive crystallization steps. Upon completion of the first step and irrespectively of the sample being crystallized through isothermal or

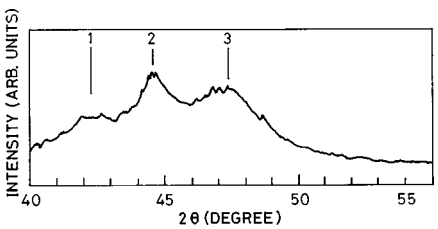

FIG. 11. X-ray-diffraction pattern corresponding to a sample with $x=11$ heat treated at 518 K for 15 h (only first step completed). Peaks 1, 2, and 3 are due to (100), (002), and (101) reflections of α-Co, respectively.

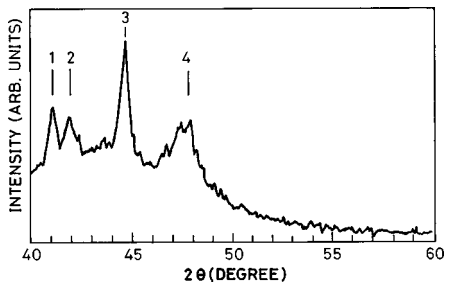

FIG. 12. X-ray-diffraction pattern corresponding to a sample with $x=11$ after full crystallization. Peak 1 corresponds to Co_2P [(121) and (201) reflections], while peaks 2, 3, and 4 correspond to peaks 1, 2, and 3 of Fig. 11, respectively.

continuous heating annealing, the x-ray diffractograms are characterized by the presence of an amorphous halo and three broad peaks that can be associated with the presence of Co. Figure 11 shows the pattern corresponding to a sample with $x=11$ after annealing for 15 h at 518 K, which resulted in the completion of the first step since no traces of it were observable in subsequent DSC scans. The most intense peak, labeled 2, can be indexed as corresponding to reflections by the (002) planes of α-Co, while peaks 1 and 3 can be indexed as (100) and (101). The intensity of these two peaks should be 0.3 and 1.66 times that of the (002) peak for isotropic samples. This indicates that the α-Co grains are preferentially oriented with the (002) direction perpendicular to the sample plane. The eventual presence of β-Co crystallites cannot be excluded since reflections from their (111) planes may also contribute to peak 2. If this were the case, the (111) direction of the crystallites would be preferentially oriented perpendicular to the plane of the samples because no other β-Co peaks are visible in the figure.

The intensity of the Co peaks increases drastically after full crystallization, the texture mentioned in the previous paragraph being clearly developed. A new peak due to (121) and (201) reflections of Co_2P becomes apparent, as can be seen in Fig. 12. The mean grain size estimated through the Scherrer formula for both Co and Co_2P is of the order of 20 nm.

The SEM observations of fresh fracture surfaces of the fully crystallized samples with $x<21$ were characterized by two main features that were already present after the completion of the first step. On the one hand, the grain size decreased gradually when moving from the region in contact with the electrolyte (''free surface'') in the deposition process towards that in contact with the substrate (''substrate surface''), as shown in Fig. 13. The maximum grain size was of hundreds of nanometers, while the minimum observable grains were close to 20 nm. On the other hand, many linear structures perpendicular to the sample plane can be observed (Figs. 13, 14, and 15). The width of these structures was up to hundreds of nanometers, and in many cases they were as long as the sample thickness.

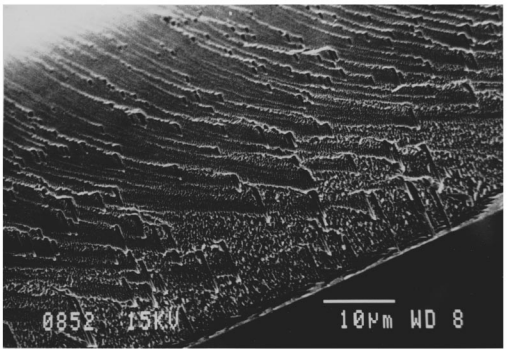

FIG. 14. SEM image of a fracture surface of a sample with $x=12.5$ crystallized by heating at 40 K min^{-1} up to 605 K (only first step completed). The grain size decreases from the ''free surface'' to the ''substrate surface,'' and sets of steps and linear structures are visible.

The XRD patterns of the crystallization product of the samples with $x>21$ also showed four peaks (Fig. 16), three of them corresponding to Co_2P. Peak 2 is the only one in this figure that can be associated with Co, probably a mixture of α and β, and, since it is very broad, reflects the presence of small grains. Peak 1 is due to diffraction by the (121) and (101) planes of Co_2P, while peak 3 (by far the most intense) can be indexed as (002). This shows that a texture with the (001) axis of the orthorhombic Co_2P structure was developed during crystallization. The mean grain size, evaluated through the Scherrer formula, is of the order of 20 nm. In contrast with the samples with lower P content, the SEM images of the fracture surfaces of crystallized samples with

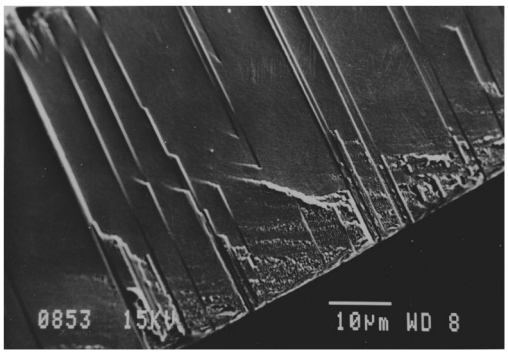

FIG. 13. SEM image of a fracture surface of a sample with $x=12.5$ crystallized by heating at 40 K min^{-1} up to 605 K (only first step completed). The fracture reveals the presence of linear structures, perpendicular to the sample surface.

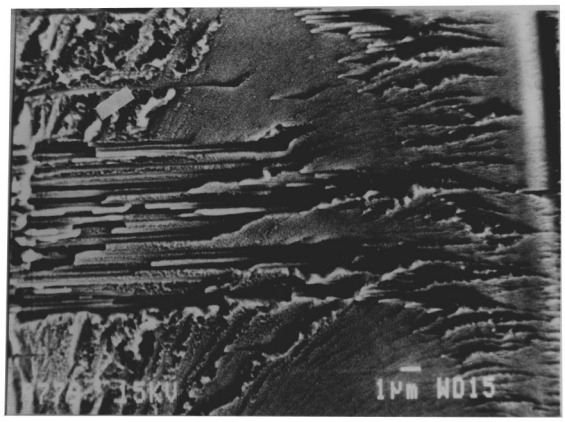

FIG. 15. Agglomeration of linear structures, perpendicular to the sample plane, in a fully crystallized sample with $x=13$.

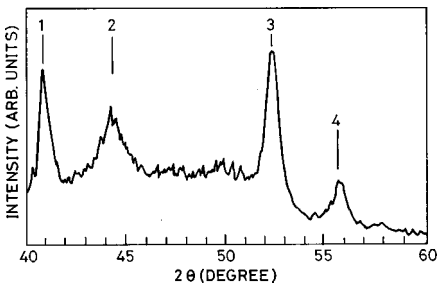

FIG. 16. X-ray-diffraction pattern corresponding to a crystallized sample with $x=23$. The most intense peaks (1, 3, and 4) are due to Co_2P, while peak 2 is due to Co crystallites.

$x>21$ showed smooth surfaces in all cases with neither granular nor linear structures present.

V. HYSTERETIC BEHAVIOR

In-plane hysteresis loops of amorphous Co-P alloys present an almost reversible region with constant susceptibility until saturation is approached, for fields of the order of 100 Oe. This is due to the rotation of the magnetization from the easy axis, perpendicular to the sample plane, towards the field direction. For fields under approximately 10 Oe, small irreversibilities are observable due to the magnetization processes in which the surface closure domains are involved.[25] These features are the same irrespectively of the composition of the sample, as shown in Figs. 17 and 18, in which the hysteresis loops of two amorphous samples with $x=13$ and $x=23$ are displayed. The origin of their easy axis being perpendicular to the sample plane lies in the growth of Co-enriched ellipsoidal structures during the deposition process.[7,8]

On the other hand, the hysteresis behavior of the crystallized samples is strongly dependent on the composition. In fact, crystallized samples with $x<21$ present loops with a constant susceptibility region until saturation is approached (see Fig. 17), which implies that the easy direction of the amorphous precursor is preserved during the crystallization process. In contrast with this, the crystallization of samples with $x>21$ induces dramatic changes in their hysteretic behavior. Figure 18 shows the hysteresis loops of a sample with $x=23$, after crystallization. A large increase in the coercive force, now being of the order of 100 Oe, and in the remanence was observed. The shape of the loop and the values of the remanence, close to half the saturation magnetization, clearly indicate that we are dealing with a polycrystalline material with high anisotropy and random crystal orientation.

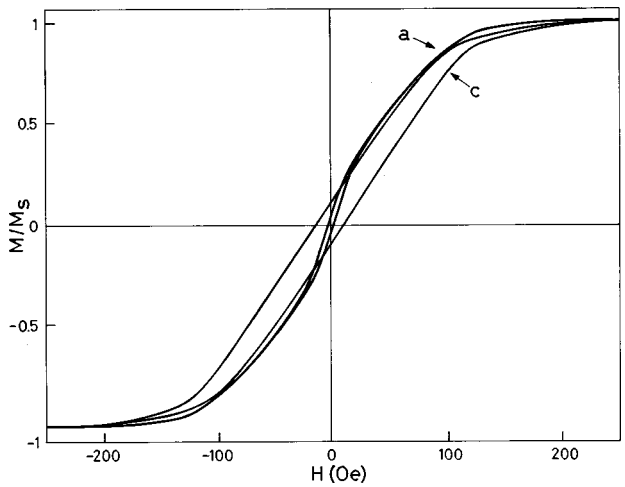

FIG. 17. Hysteresis loop of a sample with $x=13$ before (a) and after (c) crystallization.

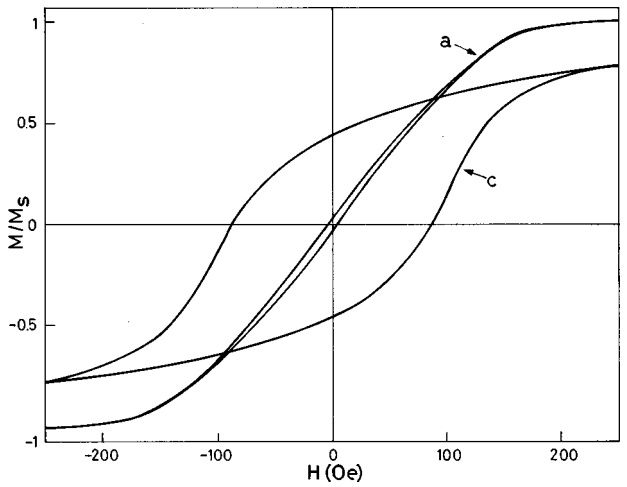

FIG. 18. Hysteresis loop of a sample with $x=23$ before (a) and after (c) crystallization.

VI. DISCUSSION OF RESULTS AND CONCLUSIONS

Analysis of the crystallization process in the Co-P amorphous system in a wide composition range allows us to propose the existence of two different crystallization mechanisms, for the samples with less than 21 at. % phosphorus and for those with more than 21 at. %.

The crystallization kinetics shows that samples with $x<21$ crystallize through two consecutive steps, the activation energy being $\sim$1.8 eV for the first and of $\sim$1.9 eV for the second steps, respectively. The frequency factor, estimated through the method proposed in the Appendix, yields values of the order of 10^{14} and 10^{13} s^{-1}, respectively. For the samples with $x>21$, crystallizing in a single step, 1.95 eV and 10^{14} s^{-1} were obtained for the activation energy and the frequency factor. It is important to note the little dispersion of the values we observed in this system in comparison with those presented in the literature, obtained by monitoring the crystallization through the thermal evolution of the resistivity[14] or the coercive force.[15]

Regarding the calculation of the T-T-T and T-HR-T diagrams for samples with $x>21$, we observe good agreement between the experimental data and the calculated curves. However, in the case of samples with two nonseparable crystallization steps and for low α values of T-T-T curves, the agreement is not quite good. This is probably caused by the impossibility of determining the crystallized fraction corresponding to each step, which, in turn, compelled us to treat both peaks as a single one.

Note that the experimental data cover a wide range of treatment conditions: from a long-term isothermal anneal to continuous heating at 80 K min^{-1}, while the calculated curves were obtained using the $f(\alpha)$ function that was de-

rived from a single scan at 10 K min^{-1} (for each composition and step). This is consistent with the kinetics being additive; that is, the crystallization rate of a sample can be expressed by means of Eq. (1) and depends exclusively on its temperature and on the amount of previously crystallized fraction. This combined with the fact that the activation energy and frequency factor values are almost independent of composition suggests that each crystallization step proceeds through a mechanism that is probably the same for all compositions, for $x<21$.

Regarding the fact that no peaks are visible in DSC runs of already fully crystallized samples, it indicates that the polymorphic α-Co$\leftrightarrow\beta$-Co transition does not happen in the Co crystallites present in the crystallization product. This transition takes place between 660 and 800 K, approximately, in pure crystalline Co, and it is strongly influenced by the previous history and grain size of the specimen.[26,27] It has been shown that mixtures of α- and β-Co normally coexist at room temperature and that it is even possible to suppress the β-Co$\rightarrow\alpha$-Co transformation upon quenching samples with a grain size below a critical value.[27] In our opinion the absence of this polymorphic transition in our crystallized samples can be attributed to their specific microstructural features. In particular, the small grain size of the Co crystallites combined with the texture of the crystallization product may inhibit the polymorphic transition or shift it to temperatures above 990 K.

In agreement with the existence of two different crystallization mechanisms dependent on the phosphorus content being either above or below 21 at. %, the microstructural analysis reveals a strong difference between the resulting crystallization products in both compositional ranges. In all cases the final product is a mixture of crystalline Co and Co_2P. However, the crystallization of samples with $x<21$ leads to the formation of linear structures and of a strong texture perpendicular to the sample plane, while these features are absent for samples with $x>21$.

The texture generated in samples with $x<21$ appears in the first crystallization step, in which α-Co crystallites are produced with their (001) axes preferentially oriented perpendicular to the sample plane. This texture is preserved after the completion of the second step, in which an increase in the Co content and the segregation of Co_2P are obtained. The linear structures and sets of steps that we observed in the micrographs are consistent with the existence of a texture. The appearance of steps is a typical feature of cleavage fractures produced by planes slipping and forming a front much wider than the grain size, which requires a good degree of orientation of the grains. In particular, the formation of ''organ tube'' structures is a characteristic of cleavage in hexagonal materials.[28]

In all studied compositional ranges, the amorphous Co-P system maintains uniaxial magnetic anisotropy, with the easy axis perpendicular to the plane of the samples. Regarding the magnetic hysteresis behavior of crystallized samples with $x<21$, the original anisotropy of the amorphous precursors is preserved during crystallization. The hysteresis loops of the final product show the presence of an easy axis perpendicular to the plane of the samples, with the anisotropy being of the same order of magnitude as that of the amorphous samples. This agrees with XRD patterns, which show the existence of a texture with the (001) axes of α-Co crystallites preferentially oriented perpendicular to the plane of the samples. These axes correspond to the easy magnetization direction of cobalt.[29] The agglomeration of these oriented crystallites may lead to the formation of the columnar structures that were usually observed in the SEM images.

In contrast with this, the hysteresis loops of the crystallized samples with $x>21$ are characterized by a random distribution of the easy axes of the Co crystallites; that is, there is no memory of the original anisotropy of the amorphous precursors. The microstructural observations for these compositions are consistent with their magnetic behavior. In fact, no texture for the Co crystallites was suggested, by both x-ray diffraction and by SEM studies.

An important point in order to understand this break in the crystallization behavior of this system is related to the compositional dependence of the Curie temperature. As shown in Fig. 1, the Curie temperature of the amorphous samples with $x>21$ is lower than that of crystallization, while it is much higher for samples with $x<21$.[10] This suggests that the magnetic order present during the crystallization of the latter may act as a polarizing agent during the diffusion of cobalt atoms. Combined with the homogeneity of the anisotropy and since the easy axis direction is the same throughout the whole sample, this gives rise to a well-defined structure with the easy axes preserved along the crystallization process. The energy associated with the polarization due to the saturation magnetization of the sample can be estimated by taking into account the Zeeman energy of the cobalt atom, with approximately $1.7\mu_B$, in the local exchange field, typically of the order 10^4 kG.[30] This results in values of the order of 0.1 eV, which explains why the uniform exchange field can be an effective polarizing agent during crystallization. In fact, since the crystallization of this system is initially accomplished at temperatures close to $T=600$ K, the thermal energy K_BT is then $\sim$0.05 eV. This would also explain why applied magnetic fields of the order of a few tesla cannot induce any texture during the crystallization of amorphous precursors in the absence of magnetic order. This is because the energy associated with cobalt magnetic moments would become of the order of 10^{-4} eV.

We should also note that the eutectic in the phase diagram of the Co-P system lies at 19.9 at. %, which is also near the break in the crystallization behavior. However, there are several reasons that suggest that this does not greatly influence the microstructure of the final product. On the one hand, the magnetic easy axis direction in the amorphous precursors is perpendicular to the sample surface; i.e., it is not a favorable direction from the point of view of magnetostatic energy. In order to preserve this direction during the crystallization of samples with $x<21$, some kind of polarizing agent would be required and it is reasonable to assume that the diffusion processes by themselves would not lead to magnetization orientations that are unfavorable from the point of view of magnetostatic energy (taking into account that magnetization is present during the crystallization). On the other hand, if we consider the recrystallization processes of binary alloys, no microstructural differences are usually observed for samples of compositions near, but respectively below and above, the eutectic.[21]

Thus our results strongly support the conjecture that the crystallization of amorphous Co-P samples, which present a high degree of homogeneity from the point of view of their composition and anisotropy, is based on a mechanism in which the presence or absence of magnetic order plays a fundamental role. The presence of magnetic order, combined with the homogeneous easy axis direction throughout most of the sample, results in an effective polarization for the diffusion of Co atoms in the crystallization. This, in turn, leads to a homogeneous texture formation.

APPENDIX

The frequency factor A, corresponding to a process whose thermal dependence is given by an Arrhenius-type relation

$$k(T)=A\ \exp(-E/K_BT), \tag{A1}$$

can be estimated, under certain restrictions, through an extension of the Kissinger method for calculating the activation energy.

As a first assumption, the proportionality between the crystallization rate $d\alpha/dt$ and the instant power measured in a DSC experiment must be considered. When heating at constant rate $r=T/t$, the maximum of the crystallization peak, occurring at a temperature T_m corresponding to a time t_m, must fulfill

$$d[d\alpha/dt]/dt=0. \tag{A2}$$

By taking into account that

$$dk(T)/dt=k(T)(Er/K_BT^2), \tag{A3}$$

the following expression can be deduced:

$$d^2\alpha/dt^2=k(T)[Er/K_BT^2]f(\alpha)+k(T)[df(\alpha)/d\alpha][d\alpha/dt]. \tag{A4}$$

If the crystallization kinetics is given by expression

$$d\alpha/dt=f(\alpha)k(T), \tag{A5}$$

then condition (A2) becomes

$$Er/K_BT_m^2+A\ \exp[-E/K_BT_m][df(\alpha)/d\alpha]_{\max}=0. \tag{A6}$$

in which $[df(\alpha)/d\alpha]_{\max}$ represents the value of $df(\alpha)/d\alpha$ when T_m is reached. By taking logarithms in Eq. (A6), the expression

$$\ln[r/T_m^2]+\ \ln[E/K_B]=\ \ln\{-A[df(\alpha)/d\alpha]_{\max}\}-E/K_BT_m \tag{A7}$$

can be obtained. It shows that a plot of $\ln[r/T_m^2]$ versus $1/T_m$ for different heating rates (Kissinger plots) is a straight line with the slope equal to $-E/K_B$. The only assumption here is that the value of $[df(\alpha)/d\alpha]_{\max}$ remains constant and independent of heating rate.

The maximum of the peaks in most crystallization processes correspond to values of the crystallized fraction around 50%. When $f(\alpha)$ is given by a JMA-type function, the value of $[df(\alpha)/d\alpha]_{\alpha=0.5}$ ranges from -0.3 to -1 when the Avrami index n varies from 4 to 1.

This allows us to estimate the value of A from Eq. (A6) by plotting $Er/K_BT_m^2$ versus $\exp[-E/K_BT_m]$, its slope then being $-A[df(\alpha)/d\alpha]_{\max}$. The two restrictions to be taken into account are that the maximum of the crystallization peaks must correspond to crystallized fractions not far from 50% and that the $f(\alpha)$ function involved in the kinetics is not very different from a JMA-type one.

[1] U. Köster and U. Herold, in *Glassy Metals I*, edited by H. Guntherodt and H. Beck (Springer, Berlin, 1981), p. 225.

[2] V. E. Martín, J. Bernardi, J. Fidler, F. Cebollada, and J. M. González, J. Alloys Compd. **191**, 127 (1993).

[3] A. Brenner, D. Wight, E. Couch, and E. K. Williams, J. Res. Natl. Bur. Stand. **44**, 109 (1950).

[4] C. Favieres, M. C. Sánchez, C. Aroca, E. López, and P. Sánchez, J. Magn. Magn. Mater. **140-144**, 591 (1995).

[5] G. Dietz, H. Bestgen, and J. Hungengerg, J. Magn. Magn. Mater. **9**, 208 (1978).

[6] G. S. Cargill, III, R. J. Gambino, and J. J. Cuomo, IEEE Trans. Magn. **MAG-10**, 803 (1974).

[7] G. C. Chi and G. S. Cargill, III, Mater. Sci. Eng. **23**, 155 (1976).

[8] J. M. Riveiro and M. C. Sánchez-Trujillo, IEEE Trans. Magn. **MAG-16**, 1426 (1980)

[9] G. Dietz, H. Bestgen, and G. Godlewsky, J. Magn. Magn. Mater. **9**, 71 (1978).

[10] R. W. Cochrane and G. S. Cargill, III, Phys. Rev. Lett. **32**, 476 (1974).

[11] F. Cebollada, J. M. González, and P. Adeva, J. Mater. Res. **8**, 105 (1993).

[12] J. M. González, F. Cebollada, A. Hernando, and M. Liniers, An. Fis. B **86**, 202 (1990).

[13] J. Flechon, A. Obaida, F. Machizaud, F. A. Kuhnast, C. Cunat, and J. Hertz, J. Non-Cryst. Solids **91**, 293 (1987).

[14] R. Sonnerberg and G. Dietz, in *Rapidly Quenched Metals V*, edited by S. Steeb and H. Warlimont (Elsevier, Amsterdam, 1985), p. 703.

[15] J. M. Riveiro, M. C. Sánchez-Trujillo, and G. Rivero, IEEE Trans. Magn. **MAG-20**, 1376 (1984).

[16] H. Bestgen, in *Rapidly Quenched Metals V*, edited by S. Steeb and H. Warlimont (Elsevier, Amsterdam, 1985), p. 443.

[17] J. Dubowik and R. Gontarz, J. Magn. Magn. Mater. **62**, 197 (1986).

[18] L. A. Chekanova, R. S. Iskhakov, G. I. Fish, R. G. Khlebopros, and N. S. Chistyakov, JETP Lett. **20**, 31 (1974).

[19] M. Avrami, J. Phys. Chem. **8**, 212 (1940).

[20] M. Avrami, J. Phys. Chem. **9**, 177 (1941).

[21] J. W. Christian, *The Theory of Transformation in Metals and Alloys* (Pergamon, New York, 1975), p. 542.

[22] S. Suriñach, M. D. Baró, J. A. Diego, N. Clavaguera, and M. T. Clavaguera-Mora, Acta Metall. Mater. **40**, 37 (1992).

[23] H. E. Kissinger, J. Res. Natl. Bur. Stand. **57**, 217 (1956).

[24] S. Suriñach, M. D. Baró, M. T. Clavaguero-Mora, and N. Clavaguera, J. Non-Cryst. Solids **58**, 209 (1983).

[25] C. Aroca, J. M. Riveiro, G. Rivero, and M. C. Sánchez, J. Magn. Magn. Mater. **15-18**, 1379 (1980)

[26] M. Hansen, *Constitution of Binary Alloys* (McGraw-Hill, New York, 1958), p. 488.

[27] W. B. Pearson, *Handbook of Lattice Spacing and Structure of Metals and Alloys* (Pergamon, London, 1958), p. 500.

[28] V. Kerlins and A. Philips, *Metals Handbook*, edited by the American Society for Metals (ASM International, Metals Park, OH, 1987), Vol. 12, p. 13.

[29] E. P. Wolhfarth, *Ferromagnetic Materials* (North-Holland, Amsterdam, 1980), Vol. I, p. 41.

[30] C. Kittel, *An Introduction to Solid State Physics* (Wiley, New York, 1976), p. 460.